A high order reduction-correction method for Hopf bifurcation in fluids and for viscoelastic vibration

J. M. Cadou, F. Boumediene, Yann Guevel, G. Girault, L. Duigou, E.M. Daya, M. Potier-Ferry

A high order reduction–correction method for Hopf bifurcation in fluids and for viscoelastic vibration

J. M. Cadou[1] · F. Boumediene[2] · Y. Guevel[1] · G. Girault[3] · L. Duigou[1] · E. M. Daya[4] · M. Potier-Ferry[4]

Abstract There are many recent studies concerning reduced-order computational methods, especially reductions by projection on a small-sized basis. But it is difficult to control the quality of the solutions if the basis is fixed once and for all. This is why we attempt to define efficient and low-cost strategies for correction and updating of the basis. These correction steps re-use previously computed quantities such as: vectors and triangulated matrices. The proposed algorithms use alternately full and reduced-size steps, allowing a strong reduction in the number of full-size tangent matrices. Two classes of applications are discussed. First, we consider an algorithm for determining Hopf bifurcation points in 2D Navier–Stokes equations, but which requires time-consuming preliminary frequency-dependent calculations. New reduction–correction procedures are applied to reduce these preliminary computations. The second application concerns the response curves of viscoelastic structures. A key point is the definition of the reduced basis. Vector Taylor series are computed within the asymptotic numerical method and the relevance of this set of vectors is analysed.

Keywords Reduced-order methods · Hopf bifurcation · Viscoelastic sandwich structures · Forced vibrations

✉ J. M. Cadou
jean-marc.cadou@univ-ubs.fr

F. Boumediene
fboumediene@usthb.dz

Y. Guevel
yann.guevel@univ-ubs.fr

G. Girault
gregory.girault@st-cyr.terre-net.defense.gouv.fr

L. Duigou
laetitia.duigou@univ-ubs.fr

E. M. Daya
el-mostafa.daya@univ-lorraine.fr

M. Potier-Ferry
michel.potier-ferry@univ-lorraine.fr

[1] Laboratoire d'Ingénierie des Matériaux de Bretagne, Université de Bretagne Sud, Rue de Saint Maudé, BP 92116, 56321 Lorient Cedex, France

[2] Laboratoire de Mécanique Avancée, Faculté de Génie Mécanique, Génie des Procédés, USTHB, El Alia, BP 32, 16111 Bab Ezzouar, Alger, Algeria

[3] Centre de recherche des Écoles de Saint-Cyr Coëtquidan, Écoles de Coëtquidan, 56381 Guer cedex, France

[4] Laboratoire d'Etude des Microstructures et Mécanique des Matériaux, UMR CNRS 7239, Université de Lorraine, Ile du Saulcy, 57045 Metz Cedex, France

1 Introduction

This paper addresses the numerical simulation of forced viscoelastic sandwich structures and Hopf bifurcation in fluid mechanics by using reduction techniques. Solutions of both of these problems are complex, leading to time-consuming computations when full-size models are used. To avoid this drawback, some reduced-order methods have been proposed. A large number of studies dealing with reduction techniques can be found in the literature. Among these reduced-order models, we can distinguish those requiring a pre-processing step, i.e. an *offline* computation, and those defining the reduced basis functions *on the fly*. In this way, Proper Orthogonal Decomposition (POD [1]) is, currently one of the most popular reduced-order techniques, requiring a pre-processing step (to determine the snapshots) which extracts a low dimensional basis. This method has been applied to compute Hopf bifurcation points in Navier–Stokes equations [2] as well as, bifurcations in the framework of a complex Ginzburg Lan-

dau equation [3] or to compute steady-state post-bifurcated solutions of the Rayleigh–Bénard problem [4]. In the latter case, the *offline* stage is followed by a greedy approach [5] instead of the POD method.

A second interesting reduced-order model is the Proper Generalized Decomposition (PGD [6,7]). This method is an *a priori* reduced-order approximation that consists of searching the unknowns in the form of a separated representation. The solution is then approximated as the sum of a moderate number of functional products. This method works very well in the case of linear problems but its application to nonlinear problems is still being developed, for example, in cases where several solutions can exist due to bifurcation [6,8].

For vibration analysis of sandwich viscoelastic structures, the numerical simulation of the response to harmonic forcing for many frequencies requires a very high computational cost especially for large-scale problems. However, numerous studies deal with reduction techniques for nonlinear vibrations of viscoelastic sandwich structures. For example, some authors [9], propose a one-mode Galerkin procedure to analyse linear and nonlinear vibrations in viscoelastic sandwich structures. Lima *et al.* [10] propose a component mode synthesis technique, Zghal *et al.* [11] use an extension of the Guyan reduction method and Bilasse and Oguamanam [12] use a modal analysis of damped and undamped structures (i.e. real and complex modes).

In this paper, we discuss couplings between reduction methods and full-size corrections. A simple coupling is presented in a recent paper by Heyman *et al.* [13] who proposed a reduction technique to compute Hopf bifurcation points. These latter are accurately determined by using a bifurcation indicator [14] linked to a Newton method (see papers [15,16] for more details). Since calculating the bifurcation indicator is the most time-consuming part of the proposed algorithm, the authors in Ref. [13] propose a reduced-order model based on the asymptotic numerical method (ANM [17]). In fact, the indicator is computed by alternately solving full and reduced size problems. Firstly, a full-size resolution is carried out with ANM providing a set of vectors from the perturbation method. Secondly, these vectors define a projection matrix which is used to compute the following steps with a reduced-order model. The accuracy of the reduced solutions is checked at each step of the calculation of the indicator and, with this method, full and reduced-size are alternately performed, leading to the sought solution.

The aim of this study is to propose better reduction techniques and apply them within a more general framework, i.e. detection of Hopf bifurcation in fluid mechanics as described in [13] and the vibration of viscoelastic sandwich structures. There are two key points in the proposed reduction–correction algorithms. First, a low-cost correction is defined by using a very cheap linear solver introduced in [18] and initially applied to nonlinear elasticity. This solver relies on two previously computed quantities: a set of vectors and a factorized matrix defining a preconditioner. This allows rapid performance of the full correction steps. The second key point is the relevance of the reduced basis that results from the full-size resolutions carried out with ANM.

In this paper, we deal with the common parts of the two applications (viscoelastic sandwich structures and Hopf bifurcation): equations to be solved (Sect. 2), nonlinear solver (ANM in Sect. 3), the reduction technique (Sect. 4) and the proposed improved reduction technique (Sect. 5). Section 6 gives a brief description of the two considered applications. The final section presents the numerical tests, concerning Hopf bifurcations and viscoelastic structures.

2 Equations to be solved

The present study is concerned with the computation of numerical solutions of the following problem:

$$\mathcal{G}(\Lambda^J) = 0 \tag{1}$$

where $\mathcal{G}$ stands for a linear or a nonlinear function of an unknown Λ^J. As this problem is solved with a continuation technique, the subscript J indicates the continuation step J. In this study, two kinds of problem (1) are considered. The first concerns the computation of Hopf bifurcation points in fluid mechanics. In this case, the operator $\mathcal{G}$ is the linear stability equation resulting from the Navier–Stokes equations. The unknown Λ then represents the bifurcation mode, the angular frequency and the critical Reynolds number: see the following references for mode details [13–15]. The second problem considered here concerns the vibration of viscoelastic sandwich structures [9,19–21] and, more particularly, forced vibrations [12,20]. In this latter case, the unknown Λ represents the displacement and the angular frequency. These two problems are solved by means of the ANM [17].

3 Linearization by asymptotic numerical method

Problem (1) is solved by the ANM [17]. In this method, the unknown Λ is then sought as an integro-power series with respect to a perturbation parameter 'a':

$$\Lambda^J = \sum_{i=0}^{P} a^i \Lambda_i^J \tag{2}$$

where Λ_0^J is assumed to be a known regular solution of Eq. 1 and P stands for the truncation order of the asymptotic expansion (2). In classical ANM, the parameter 'a' is defined with

an arc-length measure, see for example [17]. By introducing this polynomial expansion into Eq. (1) and by equating like powers of 'a', we obtain a set of linear recurrent problems defined at the truncation order equal to p by:

$$\mathcal{G}_t^{\Lambda_0^J}(\Lambda_p^J) = \mathcal{F}(\Lambda_k^J) \text{ with } 0 \leq k \leq p-1 \tag{3}$$

where $\mathcal{G}_t^{\Lambda_0^J}(\bullet)$ is the tangent operator computed at the initial point Λ_0^J. The right-hand side $\mathcal{F}(\bullet)$ depends on the previous computed solutions. All the unknowns are computed by a single matrix triangulation followed by P backward-forward substitutions. Once all the terms of polynomial expansion (2) are computed, a simple criterion allows us to determine the validity range [17]:

$$a_{\max}^J = \left(\delta \frac{\|\Lambda_1^J\|}{\|\Lambda_P^J\|}\right)^{1/(P-1)} \tag{4}$$

where δ is a small parameter (in this study equal to 10^{-6} or 10^{-7}) and the symbol $\| \bullet \|$ stands for the Euclidian norm of the vector '$\bullet$'. The definition (4) is then introduced into the expression (2) to define a new starting point, Λ_0^{J+1}, and then compute a new part of the solution branch. This defines a continuation technique based on asymptotic expansions.

In classical applications of ANM, the following step $J+1$ is carried out by solving the full-size dimension problem defined with Eq. 1. For the next step of the continuation technique used in this study, we propose linking the ANM with a reduced-order model.

4 Reduced-order method

As previously explained, we can define a projection operator, Ψ, from a full-size computation:

$$\Psi = \left[\Lambda_0^{j,\perp}, \Lambda_1^{j,\perp} \ldots, \Lambda_{\text{nred}}^{j,\perp}\right] \tag{5}$$

where the symbol $\perp$ stands for the orthonormalization of the vectors Λ_p^j. This means that the reduced basis is extracted from the previous full ANM computation. We can choose all these ANM-vectors (nred $= P$) or only a part (nred $<$ P). This projection operator defines the reduced vector λ_p^{j+1}, with the following expression:

$$\Lambda_p^{j+1} = \Psi \lambda_p^{j+1} \tag{6}$$

So by introducing the above relation into Eq. (3), and by using a Galerkin projection, we obtain the following reduced linear problem at each order of the ANM:

$$g_t^{\lambda_0^{j+1}}(\lambda_p^{j+1}) = f(\lambda_k^{j+1}) \text{ with } 0 \leq k \leq p-1 \tag{7}$$

where $g_t^{\lambda_0^{j+1}}(\lambda_p^{j+1})$ and $f(\lambda_k^{j+1})$ are the reduced tangent matrix and the reduced right-hand side, respectively. These two reduced operators are defined with:

$$g_t^{\lambda_0^{j+1}} =^t \Psi \mathcal{G}_t^{\Lambda_0^J} \Psi \text{ and } f(\lambda_k^{j+1}) =^t \Psi \mathcal{F}(\Lambda_k^j) \tag{8}$$

Once all the reduced unknowns, λ_p^{j+1}, are computed using the above equations, the full-size solutions, Λ_p^{j+1}, are then determined with Eq. (6). The validity range of these asymptotic expansions are then computed [17], yielding a new starting point for the next continuation step. This reduced-continuation scheme is performed as long as an accuracy criterion is valid. In this study, we choose the following relation:

$$\|\mathcal{G}(\Lambda^J)\| \leq \epsilon \tag{9}$$

where $\| \bullet \|$ and ϵ denote, respectively, the Euclidian norm of the vector '$\bullet$' and a chosen parameter (generally, ϵ is between 10^{-4} and 10^{-2}). Thus, if criterion (9) is not satisfied for step J, the following step $J+1$ is carried out by solving a full-size problem (Eq. 3), which then yields a new projection operator Ψ for the following steps (see Reference [13]). The reduced-basis -ANM algorithm comprises the following steps (for each continuation step J):

1. The first series initiates the basis, $\Psi = [\Lambda_0^{\perp}, \Lambda_1^{\perp} \ldots, \Lambda_{\text{nred}}^{\perp}]$.
2. Reduced-basis computations, $[\lambda_0, \ldots, \lambda_P]$.
3. Computation of the full-size solution, Λ^j, and its residual $\mathcal{G}(\Lambda^J)$.
4. When necessary ($\|\mathcal{G}(\Lambda^J)\| > \epsilon$), carry out full-size computation, $\Psi^{\text{new}} = [\Lambda_0^{\perp}, \Lambda_1^{\perp} \ldots, \Lambda_{\text{nred}}^{\perp}]$
5. Basis update, $\Psi = \Psi^{\text{new}}$, go to **2.**

This procedure is simply a conventional reduction technique, to which a precision control and a restart step have been added. Compared to the literature, the origin of the basis is the main novelty of the present reduction method. For the computation of Hopf bifurcation points, it has been shown in Reference [13] that one full-size resolution is generally followed by two or three reduced-size steps. This means that the projection operator Ψ is valid for two or three reduced steps. Hence, the aim of the present study is to increase the number of continuation steps carried out with a reduction technique. For this purpose, an iterative solver [18] is used to correct the solutions obtained with the reduction technique.

5 A new reduction–correction technique

Since we cannot expect the simple reduced-order method of Sect. 4 to remain valid during many steps, a pure reduction

technique may be not optimal. A similar observation has been made in nonlinear shell analysis, see [22]. In this respect, we propose to incorporate low-cost correction steps into the pure reduction technique. This correction can work well because it is based on the reduced basis computed during a previous ANM step as well as a full matrix triangulated in a previous step. This reduction–correction technique introduced in [18] is used here to solve iteratively the linear problems defined by (3). In other words, the ANM paths (3) can be computed using three different techniques. In the first technique, the linear problems (3) are solved by a direct method with a single triangulation for all the orders (classical ANM). In the second technique, only the reduced problems (7) are solved. A third technique is introduced by returning to an exact resolution of (3) and by combining reduced-order steps and full computations with a relatively low-cost solver. In the following, some strategies are presented to manage the transitions between these three resolution techniques.

5.1 Definition

In this section, we present the method used to improve the validity of the reduced solution. We consider the reduced solution, λ_p, as already known at the order of truncation p. This vector is the solution of the reduced problem (Eq. 7). The solution of the full-size problem at the order p, for the continuation step J, can be defined by:

$$\Lambda_p^J = \Lambda_p^{\text{red}} + \Delta\Lambda_p = \Psi\lambda_p + \Delta\Lambda_p \tag{10}$$

where $\Delta\Lambda_p$ represents the correction (or the default) of the reduced solution Λ_p^{red}. There are now two possible cases: either the reduced solution is accurate and then the vector $\Delta\Lambda_p$ is nearly equal to zero, or the reduced solution is insufficiently accurate and has to be corrected by computing the vector $\Delta\Lambda_p$. The latter is the solution of the linear problem defined in Eq. 3, which can be rewritten as follows:

$$\begin{cases} [K_T]\{\Delta\Lambda_p\} = \{F\} \\ \text{with } \{F\} = \mathcal{F}(\Lambda_k^J) - [K_T]\{\Lambda_p^{\text{red}}\} \text{ and } K_T = \mathcal{G}_t^{\Lambda_0^J} \end{cases} \tag{11}$$

Several linear solvers can be used to compute the correction $\Delta\Lambda_p$. For example, a classical conjugate gradient method can be chosen associated with a pre-conditioner. In this study, we use a linear solver recently proposed in Ref. [18] which is more efficient than the conjugate gradient method when using the same pre-conditioner. Moreover, this solver links the reduced operator and the pre-conditioning matrix, which can be easily defined in the present study. Hence, according to the method presented in Ref. [18], we can define iteration {iti of the linear solver with the following expressions:

$$\begin{cases} [\mathcal{K}_T]\{\delta\lambda_p\} = \{f\} - [C]\{\Delta\Lambda_p^{i-1}\} \\ [K^*]\{Y\} = \{F\} - [K_T]\{\Psi\delta\lambda_p + \Delta\Lambda_p^{i-1}\} \\ \{\Delta\Lambda_p^i\} = \{\Delta\Lambda_p^{i-1}\} + \{\Psi\delta\lambda_p\} + \{Y\} \end{cases} \tag{12}$$

where $[C]$, $\{f\}$ and $[K^*]$ represent the coupling matrix defined with $[C] =^t \Psi[K_T]$, the reduced right-hand side of Eq. (11) and a pre-conditioner, respectively. In this study, the pre-conditioning matrix, K^*, is the factorized matrix used in the continuation step where the projection matrix, Ψ, has been defined. It is the triangulated matrix which computes the solution of the full-size problem. The advantage of using this kind of iterative solver is the fact that all the reduced operators are already defined during the computation of the reduced part (Eq.7). For example, the projection matrix, Ψ, and the reduced matrix $[\mathcal{K}_T]$ are the same for the linear correction (Eq. 12) and for the reduced linear system (Eq. 7).

Finally, when performing the iterations (Eq. 12), either a residual criterion is satisfied or a maximum number of iterations is reached (parameter imax). We adopt the following expression for the residual criterion:

$$\frac{\|[K_T]\{\Delta\Lambda_p\} - \{F\}\|}{\|\{F\}\|} < \eta_{\text{lin}} \tag{13}$$

where η_{lin} represents the required accuracy for the linear problem (11). During the computation, the accuracy of the iterate $\Delta\Lambda_p^i$ could be improved by using convergence accelerating techniques, such as the modified minimal polynomial extrapolation method (MMPE [23]) or Padé approximants [24]. These two techniques lead to the same numerical results (see Ref. [25]) and have already been applied to accelerate the convergence of nonlinear problems [26].

The improved reduction technique, presented here, can then be summarized with the following steps:

1. The first series initiates the basis, $\Psi = [\Lambda_0^{\perp}, \Lambda_1^{\perp} \ldots, \Lambda_{\text{nred}}^{\perp}]$ and the preconditionner $[K^*] = [K_T]$.
2. Reduced-basis computations,$[\lambda_0,\ldots, \lambda_p]$.
3. Full-size corrections by a linear solver combining reduced basis and preconditioner, $\Lambda_m = \Psi\lambda_m + \Delta\Lambda_m$ with $0 \leq m \leq p$.
4. Computation of the full-size solution, Λ^j, and its residual $\mathcal{G}(\Lambda^J)$.
5. When necessary, ($\|\mathcal{G}(\Lambda^J)\| > \epsilon$), carry out full-size computation, $\Psi^{\text{new}} = [\Lambda_0^{\perp}, \Lambda_1^{\perp} \ldots, \Lambda_{\text{nred}}^{\perp}]$, $[K^*]^{\text{new}} = [K_T]$
6. Basis update and Preconditioner update, $\Psi = \Psi^{\text{new}}$ and $[K^*] = [K^*]^{\text{new}}$ go to **2.**

Note that it is not always necessary to compute all the terms of the Taylor series [27] exactly. To save computation time, it may be more efficient to calculate only the first vectors ($0 \leq \text{p} \leq \text{p}^{\text{corr}}$) by (12) and the last ones ($\text{p}^{\text{corr}} + 1 \leq \text{p} \leq \text{P}$)

Table 1 Definition of the reduced-order numerical methods evaluated in this study

	Reduction	Linear correction	Basis updated
RB [13]	√	×	×
RB+	√	√	×
RB++	√	√	√

by the pure reduction method (6) and (7). This adds a new algorithm parameter p^{corr}.

5.2 Several computing strategies

The numerical techniques presented in this paper lead to the definition of several methods to compute the unknown Λ. These methods are summarized in Table 1. The first method corresponds to a pure Reduced Basis (denoted by RB in Table 1), as proposed in Ref. [13], which alternates full and reduced-size problems. In the second method, RB+ (Reduced Basis plus correction), the reduced vector at each order, Λ_p^{red}, is corrected with the linear solver presented in Sect. 5. These reduced vectors are also corrected with the third method, RB++ (Reduced Basis plus correction plus basis update), but in this case a new basis is built at the end of the reduced step using the vectors Λ_p defined with expression (Eq. 10). So, in this method, the basis is updated on the fly at each step of the continuation method by defining a new projection matrix Ψ.

5.3 An overview of the algorithms

In the more sophisticated algorithms (RB+ and RB++), we combine three sorts of ANM-steps. We always start with full ANM-computations, where all the terms of the Taylor series are computed exactly by a direct linear solver. This provides both a reduced basis and a triangulated matrix. The next steps involve reduction techniques. In the simplest reduction technique (RB), ANM reduced steps are concatenated as long as the accuracy criterion is satisfied. When this condition fails, we return to the full computation. Within RB+ and RB++, the reduction–correction of Sect. 5.1 is applied after this second phase: this means that the linear problems are again solved with a low-cost iterative solver combining reduction and preconditioning. This procedure is stopped when the accuracy criterion is satisfied, in which case a new full computation is restarted. The difference between RB+ and RB++ corresponds to an update of the basis after each computation of a series by the reduction–correction method.

6 Numerical applications

In this section, we present the equations (Eq. 1) governing the two numerical problems studied in this paper.

6.1 Hopf bifurcation in fluid mechanics

The first application proposed in this study concerns the stability of fluid flow and, more precisely, the computation of Hopf bifurcation points in 2D Navier–Stokes equations. This kind of bifurcation characterizes the transition between a steady flow and a time-periodic solution. These bifurcation points are computed by linking a bifurcation indicator [14] to a direct method [30]. This gives an automatic and robust method to detect accurate critical Reynolds numbers [15,16]. Since calculus of the indicator is time consuming, a reduction technique is proposed in Ref. [13] to save computational time. In this study, we propose to decrease this computational time by using the improved reduction technique. A Hopf bifurcation point satisfies the following nonlinear equations:

$$\begin{cases} L(U^S) + Q(U^S, U^S) - \lambda F^S = 0 \quad \text{in} \quad \Omega \\ i\omega M(V) + L(V) + Q(v, U^S) + Q(U^S, V) = 0 \quad \text{in} \quad \Omega \\ V^{\mathbf{u}} = 0 \quad \text{on} \quad \partial_{\mathbf{u}}\Omega \\ l(V) = 0 \quad \text{in} \quad \Omega \end{cases} \tag{14}$$

where U^S, λ, ω, V represent respectively the steady solution (velocity and pressure) of the Navier–Stokes equations, the Reynolds number, the angular frequency and the bifurcation mode. The first equation of the above system (14) stands for the steady Navier–Stokes equations and the second represents the linear stability equation. The third equation is a boundary condition on the velocity part of the bifurcation mode, V. The last equation (i.e. $l(V) = 0$) is an additional expression which is introduced to have a suitably posed problem, for more detail, see references [15,28,30,31]. The symbols $L(\bullet)$, $Q(\bullet, \bullet)$ and $M(\bullet)$ stand for linear, quadratic and mass operators ([14–16]). Some authors [28,30,31] have proposed using a Newton method for solving the system (14). In the present study, as in References [15,16], we compute the Hopf bifurcation points by linking a bifurcation indicator, as introduced in [14] for fluid mechanics, with a Newton method. This indicator, denoted by ϕ in the following, has the property to be null at the Hopf bifurcation point [32]. This indicator is a scalar quantity that is introduced in the second equation of system (14):

$$\begin{cases} i\omega M(V) + L(V) + Q(V, U_F^S) + Q(U_F^S, V) - \phi f = 0 \\ V^{\mathbf{u}} = 0 \quad on \quad \partial_{\mathbf{u}}\Omega \\ l(V) = 0 \quad \text{in} \quad \Omega \end{cases} \tag{15}$$

where f is a random load vector. A Hopf bifurcation can be determined with the method proposed in [15,16] as follows. Firstly, for a fixed value of the Reynolds number, for

which U_F^S is fixed and known in Eq. (15), we can compute the variation of the indicator, ϕ, as a function of the angular frequency using ANM. Once this computation is carried out, all the minimum values of the indicator are introduced as initial guesses into the system (14) to be solved with a Newton method. This allows the automatic calculation of accurate critical Reynolds numbers. As shown in Ref. [16], the computation of the variation of the indicator as a function of the frequency is the most time-consuming part of the proposed algorithm. So, in Ref. [13], the computation of the indicator is carried out with the reduced technique presented in Sect. 4. This method is denoted by RB in Table 1.

In summary, in the case of the computation of Hopf bifurcation points, the problem expressed in (1) is represented by the Eq. (15) and the unknown Λ stands for the indicator, ϕ, and the bifurcation mode V. The perturbation parameter defined in Eq. (2) is then identified as the angular frequency ω:

$$\mathrm{a} = \omega \tag{16}$$

6.2 Vibration of viscoelastic sandwich structures

The second application concerns the analysis of the forced harmonic vibration of viscoelastic sandwich structures. The discrete equation of this kind of structure excited by a harmonic force of amplitude F, as obtained with the finite element method, can be written in the following form:

$$[\mathrm{K}_0 + E(\omega)\mathrm{K}_v - \omega^2\mathrm{M}]\mathrm{U} = \mathrm{F} \tag{17}$$

where ω is the angular frequency, U is the complex displacement, M is the mass matrix, K_0 and K_v represent two real constant stiffness matrices. This decomposition of the rigidity of the structure into two stiffness matrices is generally adopted when the material constituting the viscoelastic sandwich structure is assumed to be homogeneous and isotropic [12,20]. The symbol $E(\omega)$ denotes the complex Young's modulus of the viscoelastic core which mechanical characteristics are depending nonlinearly on the frequency ω. Two models are considered in this study: a constant Young's modulus and a Young's modulus varying as a function of circular frequency according to the generalized Maxwell model [21]. When studying viscoelastic structures, the objective is to compute the response curves over a large range of frequencies. A simple way to compute the variation of the displacement U as a function of the frequency is to generate and decompose the complex dynamic matrix of Eq. (17) for a large number values of frequency [33]. This leads to very high computational cost. In [20], the authors propose to solve the Eq. (17) by an ANM. With this method, the computational cost can be considerably reduced [20]. The improved-reduced algorithm presented here is used to compute the response curve of viscoelastic sandwich structures. Hence, the unknown Λ in Eq. (1) can be obtained in Eq. (17) where U is the displacement, ω is the angular frequency, E is the Young modulus, with this latter being assumed to be frequency dependent. The perturbation parameter, a, defined in Eq. (2) is then defined by using an arc length measure [17]:

$$a = < U - U_0, U_1 > + (\omega - \omega_0, \omega_1) \tag{18}$$

where $< \bullet, \bullet >$ stands for the Euclidian scalar product.

Table 2 Definition of user parameters for the proposed numerical methods

Classical ANM parameters	P	Order of the series. This is also the maximum dimension of the basis.
	δ	ANM end step criterion
Parameters to govern the transition between the solvers	ϵ	Residual control (to quit the pure reduced method)
	η_{lin}	Control of the convergence of the linear solver
	imax	Maximal number of iterations for the linear solver
	nred	Dimension of the projection operator
	$\mathrm{p}^{\mathrm{corr}}$	Number of vectors Λ_p^{red} corrected among P vectors.

7 Numerical results

In this section, we present the numerical tests evaluated in this study as well as the results obtained with the different strategies. Since the proposed reduced techniques involve a large number of user parameters, their descriptions are given in Table 2. For both applications, the equations to be solved (Eq. 1) are nearly the same. Nevertheless, the expected results are not exactly the same. In the case of Hopf bifurcation, the search for an indicator curve yields only a preliminary result before the iterative search of bifurcation points. In the case of viscoelastic structures, the response curve is the quantity of interest and a better accuracy is required.

7.1 Numerical tests for Hopf instabilities

In this study, we take the example of flow in a square cavity to evaluate the proposed reduction techniques to compute Hopf bifurcation. The geometry of this example is shown in figure (1). Two examples of boundary conditions are considered (Fig. 1). The first example denoted here as 1S, corresponds

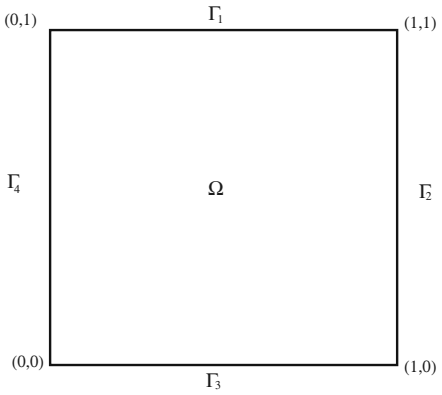

Fig. 1 Geometry and boundary conditions for a lid driven cavity

Boundary condition for 1S :
$U(x,y) = (1,0,0)$ on Γ_1
$U(x,y) = (0,0,0)$ on Γ_2, Γ_3 and Γ_4

Boundary condition for 4S :
$U(x,y) = (1,0,0)$ on Γ_1
$U(x,y) = (0,+1,0)$ on Γ_2
$U(x,y) = (-1,0,0)$ on Γ_3
$U(x,y) = (0,-1,0)$ on Γ_4

Table 3 Critical values for the first Hopf bifurcation for the two considered examples

Present results	Cavity 1 Side (1S)			Cavity 4 Sides (4S)		
	Re_c	ω_c	St_c	Re_c	ω_c	St_c
Mesh 1 (13,122 d.o.f.)	7890	2185	0.44	736	14.45	0.03
Mesh 2 (157,922 d.o.f.)	8030	2271	0.45	741	14.81	0.03
Abouhamza and Pierre [38]	8004		–			
Auteri *et al.* [39]	8018		0.44			
Boppana and Gajjar [40]	8026		0.45			
Brezillon *et al.* [15]	7890	2185	0.44			
Cazemier *et al.* [2]	7972		0.45			
Fortin *et al.* [41]	8000		0.45			
Polishenko and Aidun [42]	7763		0.45			
Wahba [43]				735 ($\pm$4)		0.09
Zhuo *et al.* [44]				721 ($\pm$6)		

to a classical lid-driven cavity where a horizontal velocity is imposed on the upper side, while velocities are equal to zero on the three other sides. In the second example, denoted here by 4S, a velocity is imposed on the four sides of the cavity as defined in the figure (1). In both cases, the Reynolds number is computed with the following expression:

$$Re = \frac{\lambda u D}{\nu} \tag{19}$$

where D is the width of the cavity (equal to 1.0), u denotes the imposed velocity on the upper side of the cavity and ν is the kinematic viscosity of the considered fluid. The Strouhal number is also introduced, being determined by the following expression:

$$St = \frac{D.\omega}{2\pi\lambda u} \tag{20}$$

For both examples, spatial discretization is performed using the finite element method [34]. A quadrilateral element is chosen with nine and three nodes for the velocity and the pressure, respectively. Details about this spatial discretization can be found in Ref. [35]. Two meshes are considered for the 1S example, one coarse (13,122 d.o.f.) and one fine (157,922 d.o.f.). For the 1S example, the first Hopf bifurcation appears with a critical Reynolds number close to 8000 and a Strouhal number near 0.45, according to results reported in the literature (see Table 3). In the case of 4S, there are fewer data available in the literature concerning critical numbers than for the 1S case. This is mainly due to the fact that a first steady bifurcation appears before the Hopf bifurcation, as reported in [36,37]. The critical Reynolds number for this steady bifurcation is close to 130. Therefore, to compute the indicator on the stable nonlinear solution branch, we choose an initial Reynolds number higher than 130. This post-bifurcation stable steady solution is obtained using the numerical method recently proposed in Ref. [45]. For this example, we find a critical Reynolds number close to 740 for the first Hopf bifurcation, which agrees well with the results reported in the literature (see Table 3).

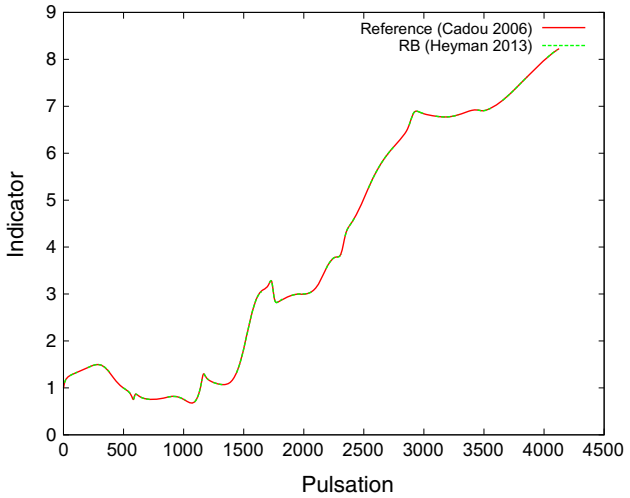

Fig. 2 Reference curve with or without reduction at Re = 6220, nred = 20, $\delta = 10^{-6}$, p = 30 and $\epsilon = 10^{-2}$. Cavity 1S

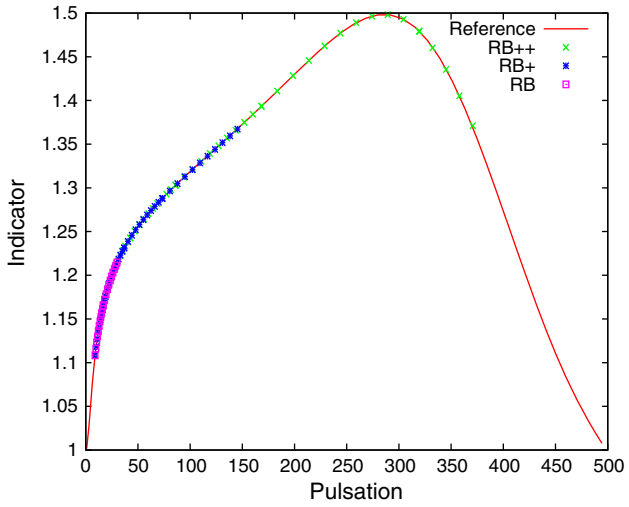

Fig. 3 Comparison of the solutions obtained with RB, RB+ and RB++ at Re = 6220, nred = 20, $\delta = 10^{-6}$, p = 30 and $\epsilon = 10^{-2}$. The figure presents the part of the response obtained with a single matrix triangulation for the three considered reduction techniques (RB, RB+ and RB++). The Reference curve requires 8 matrix triangulations. Cavity 1S

7.2 Results obtained using the proposed reduction techniques

The Hybrid method proposed in Ref. [15] is able to find Hopf bifurcation points even if the initial Reynolds number used to compute the bifurcation indicator is far from the singular points. For this reason, in the case of 1S flow, we propose to compute an indicator curve for a Reynolds number equal to 6220. We consider the coarsest mesh (Mesh 1 with 13,122 d.o.f, Table 3). In this case, the Hopf bifurcation appears when the Reynolds number is equal to 7890, which is relatively far from the Reynolds number for which the indicator curve is carried out. Figure 2 shows this indicator plotted against the angular frequency, ω. To compute this indicator, some parameters are fixed. Hence, the truncation order of the asymptotic expansion (P) and the accuracy parameter (δ) are fixed at values of 30 and 10^{-6}, respectively. The same values are used for all the indicator computations presented in this study, and represent optimum values according to the results given in Ref. [13]. The parameter ϵ for RB is chosen equal to 10^{-2}. In Fig. 2, we plot the solutions obtained with (RB [13]) or without (reference curve) the reduction technique. We can see the part of the curve (shown in green) obtained with the reduction method and also with full-size steps (shown in red). In this way, the reduction technique alternates the full-sized and reduced steps of the continuation method. The curves are obtained using 56 and 67 continuation steps for the full-size resolution (Reference) and RB, respectively (see Table 4). In the case of RB, 46 steps are carried out with the reduction techniques described here, leading to 21 full-size matrix triangulations (corresponding to the discrete tangent operator, $\mathcal{G}_t^{\Lambda_0^J}(\bullet)$ in Eq. 3) instead of 56 with the Reference solution. With smaller value of the parameter ϵ, 10^{-3} for example, the number of continuation steps with RB is equal to 66 with 26 full-size matrix triangulations and consequently 40 steps with the reduction technique.

Based on this evolution of the bifurcation indicator, we can then automatically determine initial values for the Newton method. These latter represent the minimum values of the indicator, providing us with 14 initial estimates using the curve presented in Fig. 2. These 14 values are introduced into the Newton method, yielding two bifurcation points: $\mathrm{Re_c} = 7890$ and $\mathrm{Re_c} = 11,417$. These critical values are obtained with 7 and 9 iterations of the Newton method, respectively. The same number of bifurcation points are obtained in both methods considered here if the parameter ϵ is lower or equal to 10^{-2}. The same conclusion was given in Ref. [13] (see Table 5, p. 81).

We now consider the reduced techniques defined in Table 4. In Fig. 3, we plot the value of the indicator as a function of the angular frequency for RB, RB+ and RB++, in the case of the cavity 1S and for a Reynolds number of 6220. For this example, the user parameters are imax $= 5$, $\eta_{\mathrm{lin}} = 10^{-2}$ and $\mathrm{p^{corr}} = 20$. The pre-conditioning matrix ($[K^*]$ in Eq. 12) is the full-size tangent matrix triangulated at the initial point $\omega_0 = 0$. For the reduced techniques treated here, we plot the part of the response curve obtained with only one matrix triangulation. The full-size model curve given on Fig. 3 is obtained with 8 matrix triangulations. These curves show that by using the linear solver (Eq. 12) to correct the reduced vectors, Λ_p^{red} (Eq. 10), we can considerably increase the validity range of the reduced solutions. Moreover, updating the projection matrix (Ψ) at the end of each reduced

Table 4 Performance of different numerical methods to obtain the indicator curve (Fig. 2), Re = 6220, p = 30, nred = 20, $\eta_{\text{lin}} = 10^{-2}$, P = 30, $\text{p}^{\text{corr}} = 20$, imax = 5, $\epsilon = 10^{-2}$

Method	Nb of continuation steps	Nb of matrix triangulations [K_T]	Nb of iterations of the linear solver (Eq. 12)	Nb of reduced matrices [$\mathcal{K}_T$]
Reference [14]	56	56	–	–
RB [13]	67	21	–	–
RB+	51	15	2018	46
RB++	55	8	2604	47

Cavity 1S

continuation step leads to a significant increase of the validity of the reduced solution (RB++). Hence, for angular frequencies equal to $\omega_{\text{max}}^{\text{RB}} \approx 50$, $\omega_{\text{max}}^{\text{RB+}} \approx 160$ and $\omega_{\text{max}}^{\text{RB++}} \approx 360$, the accuracy of the reduced solutions is greater than the accuracy sought ($\epsilon = 10^{-2}$). We should bear in mind that, without reduction (the Reference curve in Fig. 3), at least 7 matrix triangulations are needed to obtain an angular frequency greater than 360. Finally, the entire indicator curve can be computed with the proposed reduced techniques. This curve is obtained with 8 matrix triangulations (RB++, see Table 4) instead of 21 with RB and 56 with the full-size model. With this curve, the critical Reynolds numbers obtained are the same as previously ($\text{Re}_c = 7890$ and $\text{Re}_c = 11417$) with the same number of iterations of the Newton method.

7.3 Study of user parameters for the reduced techniques

The first parameter studied here is the maximum number of iterations, imax, which allows us to correct the reduced solution, Λ_p^{red}, using the linear solver defined by the expressions given in (12). For each order of truncation, p, of the perturbation method, we need to correct the reduced vector Λ_p^{red}. In the case of RB++, Fig. 4 gives the total number of iterations of the linear solver and the total number of matrix triangulations versus the parameter imax. The value of this parameter varies between 0 and 20. The required accuracy for the linear solver, η_{lin}, is fixed at 10^{-2}. These results concern the entire nonlinear curve for RB++ as shown in Fig. 2. The number of iterations reported in Fig. 4 corresponds to the total number of iterations required for all the continuation steps. For example, if the computation of the indicator curve requires 20 reduced continuation steps with $\text{p}^{\text{corr}} = 20$, the maximum number of iterations of the linear solver is then equal to $20*\text{p}^{\text{corr}}*\text{Niter}$, where Niter represents the number of iterations of the linear solver (Eq. 12) required to correct each vector Λ_p^{red}.

The results presented in Fig. 4 show that, with imax equal to 5, we obtain the minimum number of iterations of the linear solver for the method in question. The number of matrix triangulations is strongly reduced when the imax parameter increases from 0 to 5. For higher values of imax, there is no significant reduction in the number of matrix triangulations (i.e. decreasing by just one or two). In conclusion, by

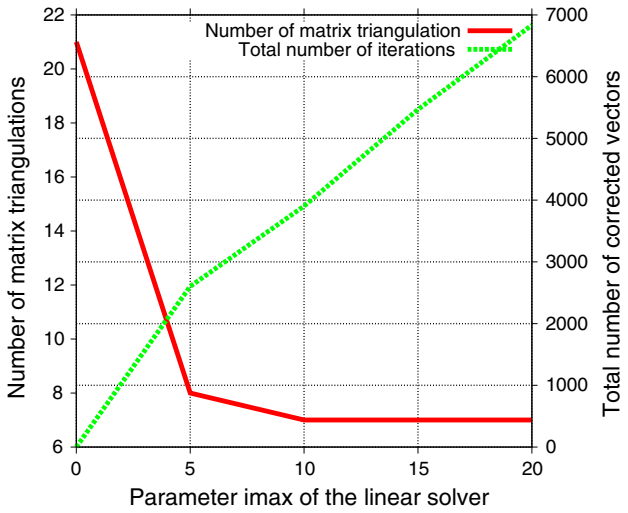

Fig. 4 Number of matrix triangulations and iterations of the linear solver plotted against the imax parameter to obtain the indicator curve of Fig. 2. nred = 20, $\eta_{\text{lin}} = 10^{-2}$, $\text{p}^{\text{corr}} = 20$ and P = 30. RB++. Cavity 1S

choosing an imax parameter close to 5, we appear to obtain an optimal value because this leads to a good compromise between the total number of iterations and matrix triangulations.

In the following, we describe the influence of the linear tolerance (accuracy of the linear solver), η_{lin}, and the number of vectors to be corrected, p^{corr}, on the total number of iterations and matrix triangulations. In Fig. 5, the number of matrix triangulations and the total number of iterations of the linear solver are plotted as a function of accuracy η_{lin}. The accuracy (ϵ in (Eq. 9)), of the reduced technique used to compute the bifurcation indicator is fixed at 10^{-2}. The results presented in Fig. 5 show that the accuracy of the linear solver has no influence on the number of matrix triangulations. The latter remains equal to 7 whatever the value of η_{lin} (with $10^{-4} \leq \eta_{\text{lin}} \leq 10^{-1}$), whereas it is no surprising that the value of parameter η_{lin} has a strong influence on the total number of iterations of the linear solver. The smallest number of iterations is obtained with the maximum value of η_{lin} (i.e. 10^{-1}). For this value of η_{lin}, the Hopf bifurcation points found are not exactly the same as those obtained using the Reference curve. For this reason, it appears preferable to

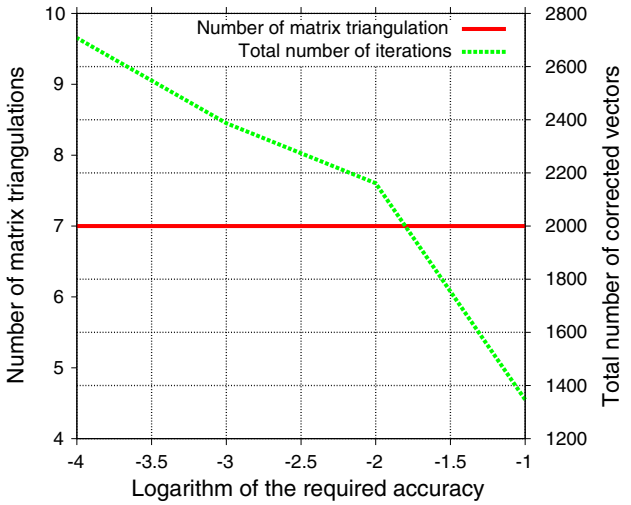

Fig. 5 Number of matrix triangulations and iterations of the linear solver plotted against required accuracy η_{lin} used to obtain the indicator curve given in Fig. 2. nred = 20, $p^{\text{corr}} = 20$, imax = 5 and P = 30. RB++. Cavity 1S

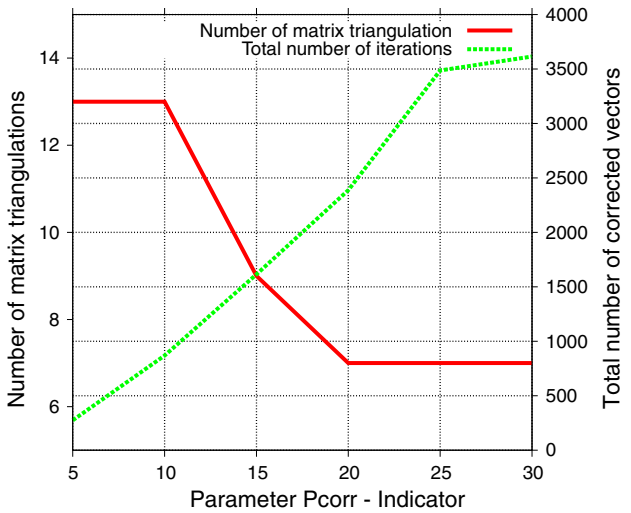

Fig. 6 Number of matrix triangulations and iterations of the linear solver as a function of the parameter p^{corr} used to obtain the indicator curve given in Fig. 2. nred = 20, $\eta_{\text{lin}} = 10^{-2}$, imax = 5 and P = 30. RB++. Cavity 1S

choose a value of η_{lin} equal to 10^{-2}. Using this value, we find the same bifurcation points after a reasonable number of iterations. The last parameter to be evaluated is the number of corrected vectors, p^{corr}. In Fig. 6, the number of corrected vectors varies from $p^{\text{corr}} = 5$ to $p^{\text{corr}} = 30$ (equal to P). The number of matrix triangulations and the number of iterations of the linear solver used to obtain the indicator curve given in Fig. 2 are then plotted against the parameter p^{corr}. The results plotted in Fig. 6 show that setting $p^{\text{corr}} = 20$ yields the lowest number of matrix triangulations and the lowest number of iterations of the linear solver. For this reason, we set the parameter, p^{corr}, in the following as equal to 20. Finally, using all the previous numerical results, we can choose optimal values for the different user parameters to compute the nonlinear indicator curve (see Fig. 2). The results are presented in Table 4. In this table, we report the number of continuation steps, the number of matrix triangulations, the number of iterations of the linear solver and the number of reduced operators to be built. The results presented in this table show that the use of a linear solver to correct the reduced solutions Λ_p^{red} leads to a stabilization of the reduced techniques based on the perturbation method. Indeed, in the case of RB, the number of steps of the continuation technique increases; the indicator curve is obtained with 67 steps, whereas 56 steps are needed with the Reference method. The two other proposed reduced techniques require 51 and 55 continuation steps for RB+ and RB++, respectively.

Another important feature is the number of matrix triangulations, corresponding to the discrete operator $\mathcal{G}_t^{\Lambda_0^J}(\bullet)$ in the full-size problem Eq. 3, which are required to obtain the indicator curve in Fig. 2. With the proposed reduced techniques, this number is considerably decreased compared to the number required with RB. Hence, 21 matrix triangulations are required with RB as against 56 without reduction (results denoted by Reference in Table 4). With RB+, 15 matrix triangulations are required. Thus updating of the reduced basis is advantageous because it decreases (in this example) the number of triangulations of full-size operators by a factor of two (8 matrix triangulations with RB++). Finally, Table 4 also reports the total number of iterations of the linear solver needed to correct the reduced solutions Λ_p^{red}. Nearly 2000 iterations are required for RB+ and around 2600 for RB++. In conclusion, RB++ seems to be the most efficient reduced technique because it associates the smallest number of matrix triangulations with a relatively small number of iterations of the linear solver (Eq. 12). In the following section, we study the gain of the computational times obtained with the proposed reduced techniques.

7.4 Computational time study for the Hopf indicator

In this section, we propose a comparison of computational times for the three presented reduced techniques. In Table 6, we give the computational times needed for each operation of the proposed numerical methods. Only the main computational times are reported in this table. Two mesh sizes are considered for the example of the lid-driven cavity: 13,122 and 157,922 d.o.f. The first study concerns the previous numerical example (cavity 1S with 13,122 d.o.f.) and the reference curve is shown in Fig. 2 (Re=6220). From results given in Table 4, the total computational time required for each method to obtain the indicator curve shown in Fig. 2 can be estimated. These computational times are deduced from data presented in Table 6. Hence, 5000s are needed with

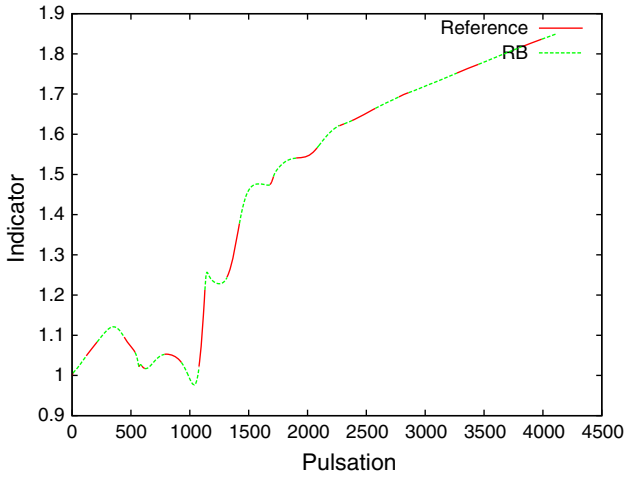

Fig. 7 Variation of the bifurcation indicator as a function of the pulsation, 1S cavity with 157,922 d.o.f, Re = 5931

ANM (Reference solution), 1800s with RB, 4200s with RB+ and 4300s with RB++. For this example with the coarsest mesh (13,122 d.o.f.), the most efficient reduction technique is RB. Indeed, RB+ and RB++ require additional operations (reduced matrices, iterations of the linear solver,...) which are numerous and finally equivalent to several matrix triangulations for this coarse mesh. For the finest mesh, the computational times needed for the matrix triangulation considerably increase and the conclusions can be different.

For this purpose, we consider two lid-driven cavity problems (1S and 4S) with a number of unknowns equal to 157,922. The critical Reynolds numbers for the first Hopf bifurcation are given in Table 3. For the 1S cavity, the indicator is computed for a Reynolds number equal to 5931. The variation of this indicator versus the pulsation is shown in Fig. 7. These curves are obtained with ANM (Reference) and RB (Fig. 7). In this example, the indicator is computed for a pulsation varying from 0 to 4100. The number of full-size matrix triangulations for each method is given in Table 5. In this table, we also give, the number of computed reduced matrices and the number of iterations of the linear solver (with RB+ and RB++) for each reduction technique. These operations are the most time-consuming (according to the results presented in Table 6). For RB+ and RB++, several values of parameter imax are considered (imax varying between 2 and 10). In Fig. 8, the indicator curve for the 4S cavity is plotted for a Reynolds number equal to 753. In this example, the range of interest for the pulsation varies from 0 to 1400. Fig. 9 presents an enlarged view of the previous figure for a pulsation varying between 10 and 20. On this figure, we can see the minimum value of the indicator which is introduced into the Newton method to obtain an accurate critical Reynolds number for the first Hopf bifurcation ($Re_c = 736$ in Table 3). The number of matrix triangulation and other data are also given in Table 5. The data in Table 5 show that RB++ stabilizes the results obtained with the reduced techniques. In fact, the number of steps of the continuation technique is nearly the same with RB++ and ANM (full-size resolution) whereas it rises with RB or RB+. As in the previous applications, RB++ requires the lowest number of matrix triangulations, with a decrease of about 80 % compared to the reference. However, in the case of RB, we note a decrease of 50 %. From the results presented in this table, we can estimate the computational times for calculating the indicator curve for each method (see Table 7). These computational times are determined by using the results presented in Tables 4, 6.

The computational times, in Table 7, represent the times required to obtain the indicator curves (Fig. 7 for 1S cavity, Re = 5931) and (Fig. 8 for 4S cavity, Re = 753). This table shows that, even with the computation of a new basis at each continuation step, RB++ provides the shortest computational times for the three reduced techniques. The time gained with this method, compared to a full model computation, is more than 60 %. As reported in Ref. [13], the gain with RB is about 40 %. With RB+, this gain is slightly lower than 60 %. By comparing RB+ with RB++, we can see that RB++ requires approximately 20 % less computational time. Therefore, for this kind of application, RB++ seems to be the best strategy.

In Table 5, we also indicate the evolution of the performances of the reduced techniques, RB+ and RB++, when parameter imax evolves between 2 and 10. Results in this table show that, for both considered examples, a great number of iterations of the linear solver does not lead to a significant decrease of the number of matrix triangulations. On the contrary, the total number of iterations to get the whole indicator curve can considerably raise up when parameter imax increases. In Table 7, the computational times needed with RB+ and RB++ for several values of parameter imax are given. These results show that choosing a value of the parameter imax lower or equal to 5, leads to the smallest computational times. This is in agreement with the conclusions stated in Sect. 7.3.

7.5 Numerical tests for viscoelastic structures

All the numerical tests concerning viscoelastic structures are performed using the sandwich element developed in [19,21]. This finite element is obtained by assembling three finite elements throughout the thickness of the structure, i.e.: two shell elements for the elastic layers [46], and a volume element for the viscoelastic core. Considering the classical assumptions used for modeling sandwich structures [47,48], the finite element so obtained is an eight-node shell element with 8 ° of freedom per node, i.e.: the longitudinal displacements of the faces,the deflection and the three rotations of the face layers. The first numerical test studied here is a cantilever beam

Table 5 Performance of the different numerical methods to obtain the indicator curves (Figs. 7 and 8), P = 30, nred = 20, $\eta_{\text{lin}} = 10^{-2}$, P = 30, $\text{p}^{\text{corr}} = 20$, $\epsilon = 10^{-2}$

Method		Nb of continuation steps	Nb of matrix triangulations $[K_T]$	Nb of reduced matrices $[\mathcal{K}_T]$	Nb of iterations of the linear solver (Eq. 12)
Cavity 1S					
ANM [14]		48	48	–	–
RB [13]		61	26	35	–
RB+	imax=2	53	19	34	714
	imax=3	53	19	34	989
	imax=5	51	20	31	1362
	imax=8	53	18	35	2192
	imax=10	53	17	36	2752
RB++	imax=2	48	12	36	1396
	imax=3	47	13	34	1519
	imax=5	47	10	37	1724
	imax=8	50	12	38	2615
	imax=10	49	10	39	2747
Cavity 4S					
ANM [14]		24	24	–	–
RB [13]		34	15	19	–
RB+	imax=2	27	9	18	378
	imax=3	29	9	20	602
	imax=5	30	9	21	956
	imax=8	28	9	19	1168
	imax=10	29	9	20	1543
RB++	imax=2	25	7	18	378
	imax=3	27	7	20	588
	imax=5	26	7	19	816
	imax=8	26	7	19	1168
	imax=10	25	6	19	1393

Cavity 1S and Cavity 4S with 157,922 d.o.f.

Table 6 Computational times (in seconds) for the different operations of the proposed algorithm

Number of d.o.f.	One full-size matrix triangulation	One linear system (Eq. 3)	One reduction matrix	One linear correction	One basis updated
13,122	58.2	1	9.4	1.2	0.0
157,922	2408	3.9	55	6.3	1.0

Considered example is the lid-driven cavity

(see Fig. 10). The beam is discretized with 160 elements and 569 nodes (4552 ° of freedom). A transverse load, with an amplitude of 100N is applied at coordinates (x = 57.79 mm, y = 6.35 mm). Two numerical tests are carried out on this beam. In the first case, we consider that the Young's modulus of the core is defined by a constant complex number: $E = E_0(1 + i\eta_c)$, where η_c is the loss factor and $i^2 = -1$. The material properties of this first example, denoted here as Beam 1, are given in Table 8. The second beam example, denoted here as Beam 2, considers a Young's modulus depending on frequency. A generalized Maxwell model is chosen with a Maxwell number of 129 and the temperature assumed for this computation is 20°C [21]. The material characteristics are also shown in Table 8.

A second kind of sandwich structure is evaluated in this study. A sandwich plate example is considered whose geometric description is given in Fig. 11. This example has been evaluated in Ref. [12]. The same finite element is used for this example. The number of degrees of freedom (d.o.f) for this example is equal to 6664 (833 nodes and 256 shell elements). The core layer is a polymer material with a constant Young's modulus ($E = E_0(1+i\eta_c)$) [12]. The material characteristics for the elastic faces and the core layer are given in Table 9. For this example, two numerical computations are

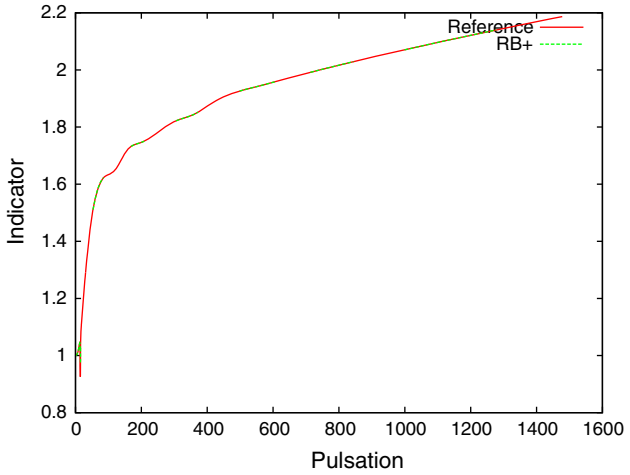

Fig. 8 Variation of the bifurcation indicator as a function of pulsation, 4S cavity with 157,922 d.o.f, Re = 753

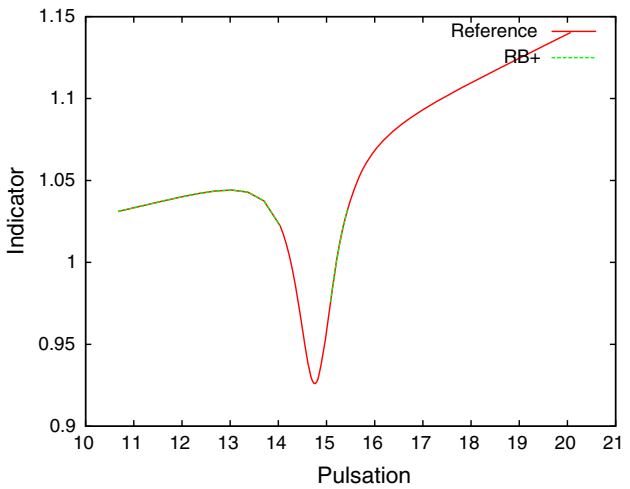

Fig. 9 Variation of bifurcation indicator as a function of pulsation, cavity 4S with 157,922 d.o.f, Re = 753. Enlarged view of Fig. 8

carried with different applied boundary conditions: SSSS or CFCF. In the latter case, the clamped sides are y = 0 mm and y = 304.8 mm. Symbols 'S', 'C' and 'F' stand for simply supported, clamped and free respectively. For the SSSS, the core loss factor, η_c is taken as equal to 0.7, whereas this parameter is equal to 0.5 for CFCF. For both studied plates, an harmonic load is applied at $x = \frac{L}{4}$ and $y = \frac{l}{4}$ with an amplitude equal to 2000N.

7.6 Numerical results for viscoelastic structures

In the numerical tests carried out for examples of viscoelastic structures, almost all the values of the user parameters are fixed. Hence, the truncation order P is equal to 20 (with p^{corr} = 20 for RB+ and RB++), while the "small" parameter, δ, which is used to compute the validity range of the asymptotic expansions is equal to 10^{-7}. The projection matrix, Ψ, used for the reduced techniques is defined by a number of vectors, nred, taken as equal to 20. For the linear solver, the maximum number of iterations, imax, is equal to 2 or 3 and the value $\eta_{lin} = 10^{-2}$ is chosen for the required accuracy. All these values are chosen according to the analysis carried out for the computation of the bifurcation indicator as described

Table 7 Computational times required to obtain the indicator curves (Fig. 7 for 1S cavity, Re = 5931) and (Fig. 8 for 4S cavity, Re = 753), P = 30, nred = 20, $\eta_{lin} = 10^{-2}$, P = 30, $p^{corr} = 20$, $\epsilon = 10^{-2}$

Method	Computational times (s)	
	Cavity 1S	Cavity 4S
ANM [14]	12,1200	60,600
RB [13]	68,989	34,207
RB+ (imax=2)	54,804	26,259
RB+ (imax=3)	53,635	27,835
RB+ (imax=5)	61,217	30,120
RB+ (imax=8)	61,620	31,291
RB+ (imax=10)	62,600	33,708
RB++ (imax=2)	43,054	21,817
RB++ (imax=3)	46,135	23,304
RB++ (imax=5)	40,162	24,685
RB++ (imax=8)	48,079	26,903
RB++ (imax=10)	46,525	25,826

Mesh with 157,922 d.o.f.

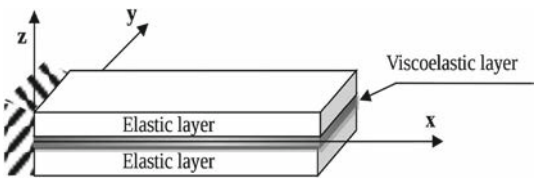

Fig. 10 Geometric description of sandwich beam with dimensions L = 177.8 mm and l = 12.7 mm. The load F is positioned at x = 57.79 mm and y = 6.35 mm with an amplitude of 100N

Table 8 Material properties of the sandwich beams (Fig. 10)

Material properties	Elastic layers	Viscoelastic layer
Beam 1		
Young's modulus	$E_e = 6.9\,10^{10}$ N/m^2	$E_0 = 1794\,10^3$ N/m^2
Poisson's ratio	$\nu_e = 0.3$	$\nu_v = 0.3$
Density	$\rho_e = 2766$ kg/m^3	$\rho_v = 968.1$ kg/m^3
Thickness	$h_e = 1.524$ mm	$h_v = 0.127$ mm
Beam 2		
Young's modulus	$E_e = 2.1\,10^{11}$ N/m^2	$E_0 = 27.216\,10^6$ N/m^2
Poisson's ratio	$\nu_e = 0.3$	$\nu_v = 0.44$
Density	$\rho_e = 7800$ kg/m^3	$\rho_v = 1200$ kg/m^3
Thickness	$h_e = 1.524$ mm	$h_v = 0.127$ mm

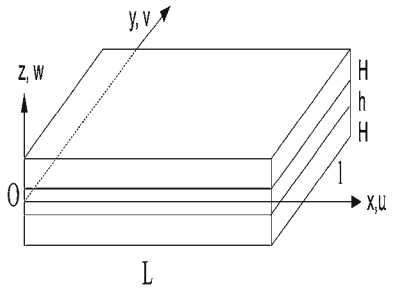

Fig. 11 Geometric description of sandwich plate with L = 348 mm and l = 304.8 mm. An excitation force is applied at $x = \frac{L}{4}$ and $y = \frac{l}{4}$ with an amplitude of 2000N

Table 9 Material properties of the sandwich plate (Fig. 11), according to example presented in Ref. [12]

Material properties	Elastic layers	Viscoelastic layer
Young's modulus	$E_e = 6.89\,10^{10}$ N/m^2	$E_0 = 2670.08\,10^3$ N/m^2
Poisson's ratio	$\nu_e = 0.3$	$\nu_v = 0.49$
Density	$\rho_e = 2740$ kg/m^3	$\rho_v = 999$ kg/m^3
Thickness	$h_e = 0.762$ mm	$h_v = 0.254$ mm

in the previous sections. The only variable parameter is the nonlinear tolerance (i.e. parameter ϵ defined in Eq. 9). The first computation is performed for Beam 1. In Fig. 12, the transverse displacement at the loaded point is plotted against the frequency. These response curves are obtained using a full-size resolution with ANM (denoted by 'ANM - Reference' in Fig. 12) and with RB and RB+ (defined in Table 1). These curves are plotted for a frequency range from 0 to 1000 Hz. The first three bending modes are obtained. For these computations, the parameter ϵ is 'large' and equal to 10^1. Due to this high value of ϵ, only one matrix triangulation is required to obtain the response curves with RB and RB+ (also with RB++ but not shown in this figure), whereas the reference curve with ANM is established using 57 matrix triangulations (see results in Table 10). This matrix triangulation is carried out at the first step of the computation for a frequency equal to zero. In Fig. 13, the logarithm of the norm of the residual vector ($\|\mathcal{G}(\Lambda^J)\|$, Eq. 1) is plotted against frequency for the three reduced techniques and for the ANM.

This plot shows that the accuracy obtained with RB is only valid over a small frequency range (lower than 100 Hz) around the first bending mode. On the contrary, RB+ and RB++ yield accurate results over a large range of frequency. The three first bending modes are then computed with an accuracy never greater than 10^{-2} for these two reduced methods. Moreover, the norm of the residual vector obtained with RB++ never exceeds 10^{-4}. We should bear in mind that only one matrix triangulation is performed to obtain this quality of solution. In Fig. 14, the logarithm of the residual vector is plotted versus frequency using an accuracy parameter ϵ equal

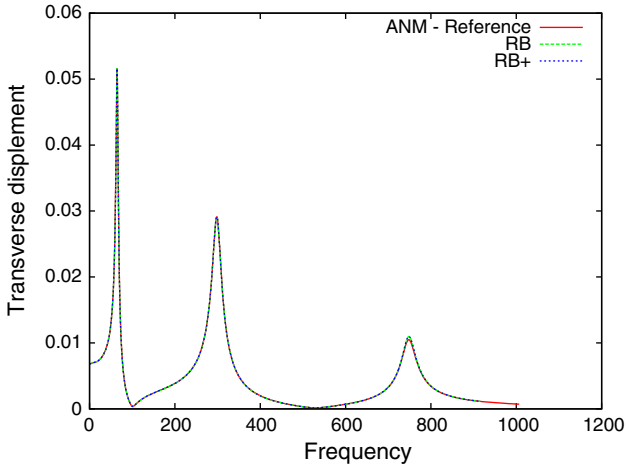

Fig. 12 Variation of transverse displacement (mm) at the excitation point as a function of frequency (Hz). Beam 1, assuming constant Young's modulus with $\eta_c = 0.3$. Parameter ϵ is equal to 10^1 in Eq. (9)

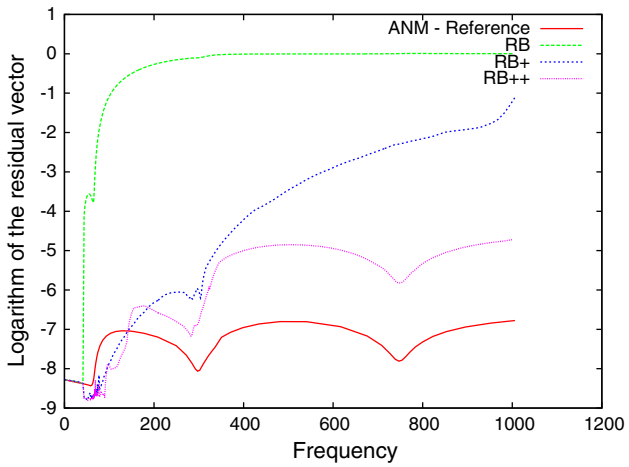

Fig. 13 Variation of logarithm of the residual vector as a function of frequency (Hz) obtained with four methods. Beam 1, assuming constant Young's modulus with $\eta_c = 0.3$. Only one matrix triangulation is carried out for the reduced techniques, RB, RB+ and RB++. Parameter ϵ is equal to 10^1 in Eq. (9)

to 10^{-3} for the three reduced techniques. Results obtained with RB++ are exactly the same as those plotted in Fig. 13, because the quality of the solution obtained with this method is never greater than 10^{-3}. In Table 10, we give the number of matrix triangulations required for each computational techniques for this value of ϵ. Hence, ANM (the reference curve in Fig. 14) requires 57 matrix triangulations (57 steps of the continuation technique) to obtain the response curve of Fig. 13, whereas RB, RB+ and RB++ require 22, 2 and 1, respectively. Thus without correction of the reduced solution Λ_p^{red}, RB decreases the number of full size matrix triangulations by a factor of two. The same efficiency is reported in the case of computation of the Hopf bifurcation indicator (see [13]). The use of the iterative method, RB+ or RB++,

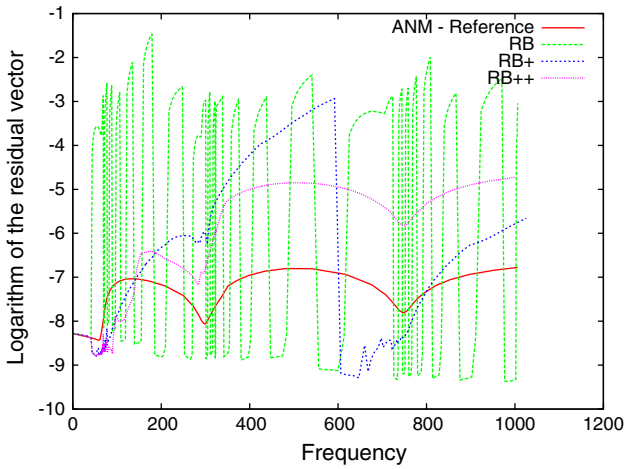

Fig. 14 Variation of logarithm of the residual vector as a function of frequency (Hz) obtained with three methods. Beam 1, assuming constant Young's modulus with $\eta_c = 0.3$. A new matrix triangulation, with RB and RB+, is performed when Eq. (9) is not satisfied with $\epsilon = 10^{-3}$. Only one matrix triangulation is required with RB++

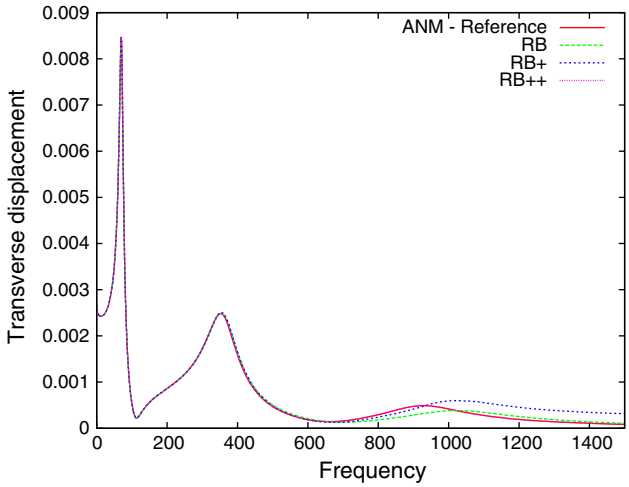

Fig. 15 Variation of transverse displacement (mm) at the excitation point as a function of frequency (Hz). Beam 2, with Young's modulus depending on frequency. Only one matrix triangulation is carried out for the reduced techniques, RB, RB+ and RB++. Parameter ϵ is equal to 10^1 in Eq. (9)

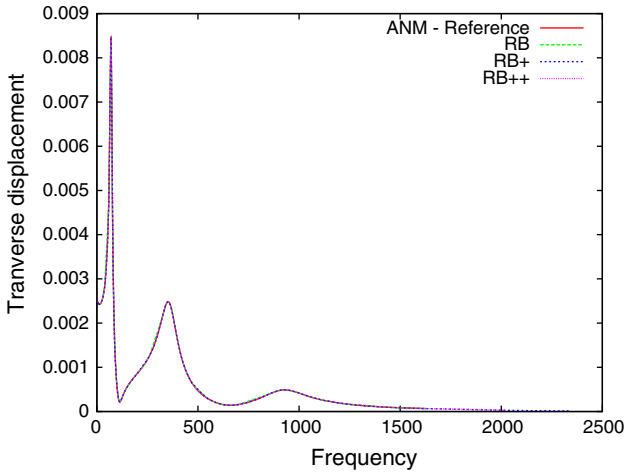

Fig. 16 Variation of transverse displacement (mm) at the excitation point as a function of frequency (Hz). Beam 2, with Young's modulus depending on frequency. Parameter ϵ is equal to 10^{-3} in Eq. (9)

considerably decreases the required number of matrix triangulations (2 or 1). Nevertheless, the computation of a new projection matrix, Ψ, at the end of each continuation step (RB++) would not appear to be so attractive in this example. Indeed, RB+ requires only one additional matrix triangulation compared to RB++. However, according to the results presented in Table 10, more than 50 basis updates are performed with RB++ to compute the response curve given in Fig. 12. Finally, this can lead to an increase of the computational time when using RB++ (compared to RB+).

We can now consider the case of Young's modulus depending on frequency (Beam 2). The response curves and the logarithm of the norm of the residual vector versus frequency are plotted in Figs. 15 and 17, respectively. In this example, the frequency range of interest is between 0 and 1500 Hz. Three bending modes are then computed with this value of frequency.

In this example, when parameter ϵ is large and equal to 10^1, the response curve obtained with the reduced techniques are not exactly the same as those obtained with ANM (Reference curve in Fig. 17) around the third mode. Only the displacement obtained with RB++ seems to be in good agreement with the displacement obtained with ANM for higher frequencies. This is also illustrated by the variation of the logarithm of the residual as a function of the frequency (see Fig. 17). The results presented in this figure show that the accuracy obtained with RB++ is once again better than that obtained with the two other reduced techniques. It is noteworthy that these response curves, for the three reduced techniques, are obtained with a single matrix triangulation carried out with a frequency equal to zero. As for Beam 1, we can control the quality of the computations by requiring a better accuracy, for example by choosing $\epsilon = 10^{-3}$ (the corresponding response curve is shown in Fig. 16). In Fig. 18, we plot the logarithm of the residual versus frequency using this value of parameter ϵ. Table 10 also gives the number of matrix triangulations required to plot these curves for all the computational techniques evaluated here.

For this numerical test, the three reduced methods are efficient compared with the reference method (ANM). The number of matrix triangulations required to compute the response curve in Fig. 15 is only equal to 7 with RB, whereas 43 triangulations are needed with the reference method. RB+ and RB++ require nearly the same number of matrix triangulations respectively 5 and 3 (Table 10).

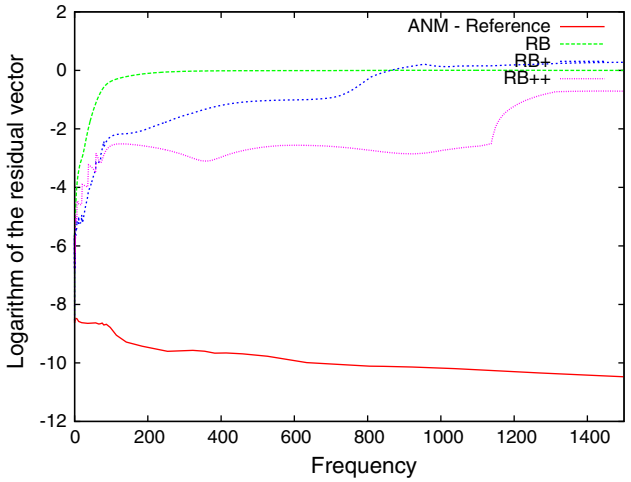

Fig. 17 Variation of logarithm of the residual vector as a function frequency, obtained with four methods. Beam 2, with Young's modulus depending on frequency. Only one matrix triangulation is carried out for the reduced techniques, RB, RB+ and RB++. Parameter ϵ is equal to 10^1 in Eq. (9)

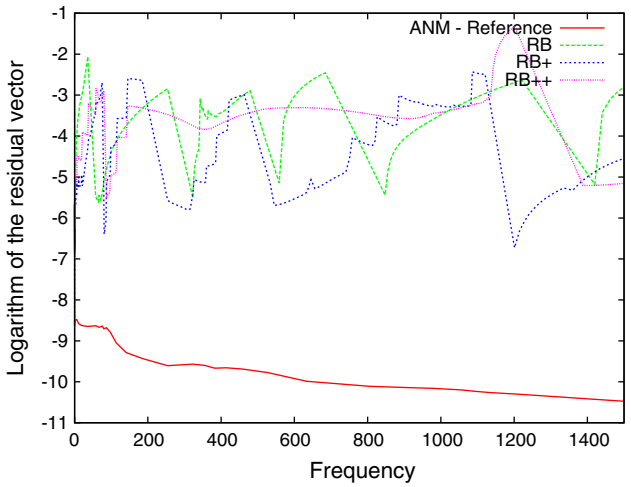

Fig. 18 Variation of the logarithm of the residual vector as a function of frequency (Hz), obtained with four methods. Beam 2, with Young's modulus depending on frequency. A new matrix triangulation, with RB, RB+ and RB++, is performed when Eq. (9) is not satisfied with $\epsilon = 10^{-3}$

7.7 Study of computational time for the viscoelastic beams

This part is devoited to the study of computational times required for each reduction technique to compute the response curves. The two previous viscoelastic beams are considered. For this study, a new mesh composed of 25,000 d.o.f. is proposed. The performance of all the reduced techniques to get the response curves for both examples are given in Table 10. The results are indicated in parenthesis in this table. As for the computation of the Hopf indicator (Sect. 7.4), the computational times for the different steps of the numerical methods are given in Table 11. These computational times linked with the results presented in Table 10 permit to estimate the total computational times needed to obtain the response curves (Beam 1 Fig. 12 and Beam 2 Fig. 15). These computational times are given in Table (12) for several values of the nonlinear tolerance (parameter ϵ). Results presented in this table show that with a moderate value of this parameter, $\epsilon = 10^{-3}$, the gain in computational times obtained with RB+ or RB++ is more than 90 % compared with a full-size computation (denoted by Reference in Table 12). This conclusion is valid for the two considered beams. Compared to the reduced technique RB, the gain obtained by using RB+ or RB++ is about 80 %. For these examples and for this value of the nonlinear accuracy parameter, the reduced technique leading to the lowest computational times is RB++. The same conclusions can be drawn when the value of the pamameter ϵ is chosen equal to 10^{-5}. If the value of the parameter ϵ is eqaul to the value adopted for the full-size computation (it means $\epsilon = 10^{-7}$ for Beam 1 and $\epsilon = 10^{-8}$ for Beam 2), the total computational times with RB+ or RB++ increase but remain lower than the times required with a full-size resolution. By considering the example Beam 1, the gain in computational time is about 80 % with RB+ and 75 % with RB++. For Beam 2, the gain, with RB+ and RB++, is lower (close to 50 %) and is the same that the one obtained with RB. Let's recall that this problem (Beam 2) is more difficult due to the fact that the Young's modulus depends on frequency.

By only considering RB+ and RB++, the gain in computational times is more important with RB++ than with RB+ for 3 computations. The number of computations presented in Table 12 is equal to 6, corresponding to 3 values of the parameter ϵ for Beam 1 and Beam 2. This result shows that the computation of a new projection matrix Ψ at the end of each continuation step is not always so attractive. Nevertheless, only 2 calculus carried out with RB+ lead to lowest computational times than the one obtained with RB++. In these cases, the gain obtained with RB+ (compared to RB++) is about 20 %.

7.8 Viscoelastic sandwich plates

We now consider sandwich plates whose geometric and material characteristics are given in Fig. 11 and Table 9, respectively. In this example, two boundary conditions are chosen: SSSS and CFCF. The response curves obtained with RB+ are plotted in Fig 19 (SSSS) and Fig. 20 (CFCF). On these figures, we also give the solution obtained in Ref. [12] showing the good agreement of RB+. For this latter technique, the parameter governing the upgrading of the reduced basis, ϵ, is chosen as equal to 10^{-2} or 10^{-3}. For these examples, the authors in Ref. [12] also use a reduced technique linked with the ANM. The present work and Ref. [12] differ in the choice of vectors defining the projection matrix

Table 10 Performance of different methods to obtain the response curves, nred=20, $\eta_{\text{lin}} = 10^{-2}$,imax = 3

Method		N1	N2	N3	N4	N5
Beam 1, response curve in Fig. 12.						
Reference (ANM)		57 (49)	57 (49)	–	–	–
RB [50]	$\epsilon = 10^{-3}$	62 (49)	22 (20)	22 (20)	40 (29)	-
	$\epsilon = 10^{-5}$	59 (49)	31 (26)	31 (26)	28 (23)	–
	$\epsilon = 10^{-7}$	59 (49)	31 (26)	31 (26)	28 (23)	–
RB+	$\epsilon = 10^{-3}$	54 (48)	2 (3)	3 (3)	51 (45)	1126 (959)
	$\epsilon = 10^{-5}$	54 (49)	4 (4)	4 (4)	50 (45)	1062 (943)
	$\epsilon = 10^{-7}$	54 (48)	8 (8)	8 (8)	46 (40)	990 (841)
RB++	$\epsilon = 10^{-3}$	57 (55)	1 (2)	55 (53)	55 (53)	1167 (1130)
	$\epsilon = 10^{-5}$	54 (54)	3 (3)	51 (51)	51 (51)	1083 (1088)
	$\epsilon = 10^{-7}$	62 (50)	9 (10)	53 (40)	53 (40)	1134 (843)
Beam 2, response curve in Fig. 15.						
Reference (ANM)		43 (42)	43 (42)	–	–	–
RB [50]	$\epsilon = 10^{-3}$	43 (44)	7 (10)	7 (9)	36 (34)	–
	$\epsilon = 10^{-5}$	43 (43)	15 (16)	15 (16)	28 (27)	–
	$\epsilon = 10^{-8}$	43 (43)	22 (22)	22 (21)	21 (21)	–
RB+	$\epsilon = 10^{-3}$	45 (42)	5 (4)	5 (4)	40 (38)	1270 (1092)
	$\epsilon = 10^{-5}$	47 (40)	10 (8)	10 (8)	37 (32)	838 (856)
	$\epsilon = 10^{-8}$	43 (43)	22 (21)	22 (21)	21 (22)	441 (505)
RB++	$\epsilon = 10^{-3}$	47 (48)	3 (2)	44 (46)	44 (46)	1280 (1273)
	$\epsilon = 10^{-5}$	48 (45)	12 (9)	36 (36)	36 (36)	822 (1010)
	$\epsilon = 10^{-8}$	43 (43)	22 (22)	21 (21)	21 (21)	441 (531)

Symbols N1, N2, N3, N4 and N5 stand for the number of steps of the continuation technique, the number of matrix triangulations [K_T], the number of basis updates, the number of reduced matrices [$\mathcal{K}_T$] and the number of iterations of the linear solver (Eq. 12) respectively. In parenthesis, results are obtained with a finer mesh (25 000 d.o.f.)

Table 11 Computational times (in seconds) for the different operations of the proposed algorithm

One full-size matrix triangulation	One linear system (Eq. 3)	One reduction matrix	One linear correction	One basis updated
14000	2.6	40	12	0.01

Considered examples are Beam 1 and Beam 2 with a finer mesh (25,000 d.o.f.)

Ψ. In Ref. [12], these vectors are obtained by solving the eigenvalue problem either of the undamped or of the viscoelastic (complex eigenvalue problem) structure for the free-vibration problem defined in Eq. 17 with F equal to zero. In Ref. [12], the number of vectors (parameter nred in this study) of the projection matrix varies from 5 to 150. These reduced solutions are compared to those obtained with a full-size computation carried out with the ANM, as in this study. The results in Ref. [12] show that the number of vectors of the projection matrix must be greater than 50 to give solutions in good agreement with the reference ones. In this reference [12], the authors only present displacement curves versus frequency. Thus it is rather difficult to compare the accuracy of the solutions obtained using the proposed reduction techniques with those of Ref. [12]. Nevertheless, the number of vectors of the projection matrix is smaller in our study (nred = 20), whereas more than 50 vectors are required with a real basis or a complex basis [12]. In Table 13, we report the number of full-size matrix triangulations required for the three reduced techniques and a full-size resolution for both plates. The results are obtained with parameter ϵ equal to 10^{-3} (in parenthesis for $\epsilon = 10^{-2}$). This table shows that the proposed reduced techniques lead to a decrease in the number of matrix triangulations, compared to the ANM computations, amounting to nearly 50 % with RB, and 90 % with RB+ and RB++. Results with RB are similar to those obtained in the case of the bifurcation indicator (see Table 4 or results in Ref. [13]). Table 13, also shows that, for both studied plates, RB+ and RB++ require the same number of matrix triangulations. According to those

Table 12 Total computational times (in seconds) to obtain the curves of Fig. 12 (Beam 1) and Fig. 15 (Beam 2) with a finer mesh (25,000 d.o.f.) according to the results presented in Tables 10 and 11

Method	Beam 1	Beam 2
Reference (ANM)	690,000	590,000
RB [50]		
$\epsilon = 10^{-3}$	282,000	85,800
$\epsilon = 10^{-5}$	366,000	212,000
$\epsilon = 10^{-7}$	366,000	–
$\epsilon = 10^{-8}$	–	310,000
RB+		
$\epsilon = 10^{-3}$	55,500	70,800
$\epsilon = 10^{-5}$	69,300	124,000
$\epsilon = 10^{-7}$	124,000	–
$\epsilon = 10^{-8}$	–	316,000
RB++		
$\epsilon = 10^{-3}$	43,800	45,200
$\epsilon = 10^{-5}$	57,300	140,000
$\epsilon = 10^{-7}$	152,200	–
$\epsilon = 10^{-8}$	–	316,300

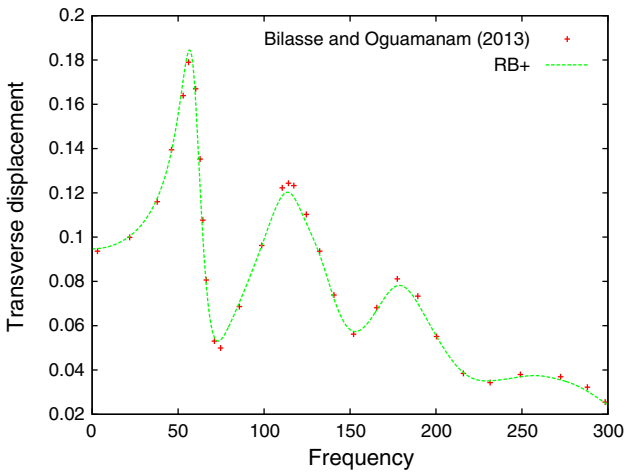

Fig. 19 Variation of transverse displacement (mm) at the excitation point as a function of frequency (Hz). SSSS sandwich Plate [12], constant Young's modulus with $\eta_c = 0.7$. Parameter ϵ is equal to 10^{-2}

results, it seems that the best reduced technique for this kind of application is RB+. Indeed, this latter leads to considerable decrease in the number of matrix triangulation without updating the projection operator Ψ at the end of each continuation step. However, with RB++, a new projection operator is computed at each step without significantly decreasing the number of full-size matrix triangulations (compared to RB+).

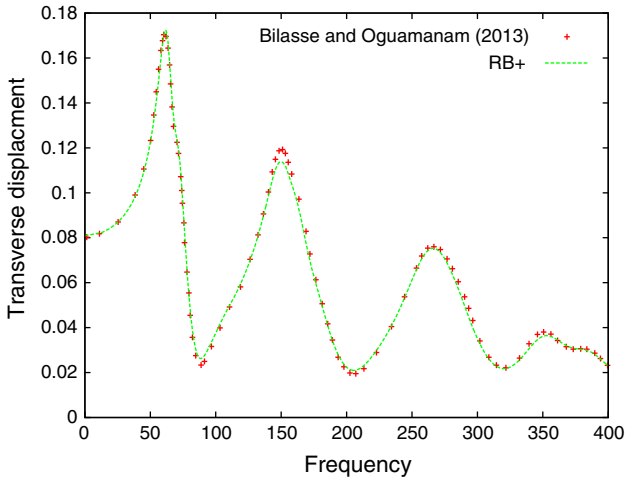

Fig. 20 Variation of transverse displacement (mm) at the excitation point as a function of frequency (Hz). CFCF sandwich Plate [12], constant Young's modulus with $\eta_c = 0.5$. Parameter ϵ is equal to 10^{-2}

Table 13 Comparison of the number of matrix triangulations for the viscoelastic sandwich plates

Method	Number of continuation steps	Number of matrix triangulations
SSSS Plate, response curve in Fig. 19		
ANM	70	70
RB	71 (72)	20 (15)
RB+	77 (74)	4 (3)
RB++	75 (74)	4 (3)
CFCF, response curve in Fig. 20		
ANM	53	53
RB	53 (53)	27 (24)
RB+	53 (53)	5 (3)
RB++	53 (51)	5 (3)

Parameter ϵ is equal to 10^{-3} in Eq. (9) (in brackets results with $\epsilon = 10^{-2}$)

8 Conclusion

This paper discusses the introduction of correction phases in Galerkin reduced-order projection methods. In the literature, the projection basis is generally built from time-consuming preliminary computations followed by Proper Orthogonalized Decomposition to reduce the size of the basis. On the other hand, the accuracy of a simplified method may be limited by using a "frozen" basis. The challenge here is to define a low-cost correction procedure, which is made easier by using the ANM where previously computed vectors and matrices provide relevant projection operators and preconditioners. More precisely, these corrections can be performed with a low-cost iterative linear solver as recently proposed by [18]. This reduction–correction technique is applied to two

classes of frequency-dependent problems over a wide range of frequencies, i.e.: detection of Hopf bifurcation points in fluid mechanics and the vibration of viscoelastic sandwich structures (beams and shells). In this study, we provide many numerical examples and discuss the advantages of correction phases and basis updates. The speed-up obtained with the correction phases greatly depends on the requested accuracy, parameter ϵ. For the computation of Hopf bifurcation, the value of the parameter is chosen equal to 10^{-2} (according to the conclusion given in Ref. [13]). For this value, the same bifurcation points are obtained with the full-size computation and the reduced techniques presented in this paper. For this kind of problem, the computational time reduction, compared to a full-size computation, is about 50 % with RB+ and 60 % with RB++. Compared with the initial reduced method, RB presented in Ref. [13], the computation time reduction is close to 15 and 35 % for RB+ and RB++ respectively. When considering the vibration of viscoelastic sandwich structures, the accuracy of the response curve is quite important. Hence, the gain in computational time obtained with the proposed reduced techniques clearly depends on the parameter ϵ. For moderate values of ϵ (10^{-3}), the response curve, with RB+ and RB++, is obtained with a significant decrease of the computational time compared to a full-size computation (about 90 %). When the accuracy, required with RB+ or RB++, is the same that the ones obtained with a full-size computation, the gain is about 50 %. In this case, the three reduced techniques (RB, RB+ and RB++) need the same computational times which are two times lower than those obtained with a full-size computation. The advantage of using basis updates is not so evident because they increase the number of reduced problems. However, according to our tests, the most efficient algorithm combines basis reduction using ANM with correction phases and basis updates. It is evident that an arbitrary interval of frequency cannot be accounted for in a single step, and few full updates including matrix updates are generally needed. Even so, the number of full matrix updates remains small compared with pure continuation method. The proposed procedures lead to improved continuation methods for the dynamic response of viscoelastic structures and the detection of Hopf bifurcations. It is likely that these procedures could be extended to path-following techniques for nonlinear problems as initially developed in [18,49].

Acknowledgments El Mostafa Daya and Michel Potier-Ferry gratefully acknowledge the financial support of the French National Research Agency ANR (Labex DAMAS, Grant No. ANR-11-LABX-0008-01).

References

1. Lumley JL (1967) The structure of inhomogeneous turbulent flows. In: Yaglom AM, Tatarski VI (eds) Atmospheric turbulence and radio wave propagation. NAUCA, Moscow
2. Cazemier W, Verstappen RWCP, Veldman AEP (1998) Proper orthogonal decomposition and low-dimensional models for driven cavity flows. Phys Fluids 10–7:1685–1699
3. Terragni F, Vega JM (2014) Construction of bifurcation diagrams using POD on the fly. SIAM J Appl Dyn Syst 13(1):339–365
4. Herrero H, Maday Y, Plaa F (2013) RB (Reduced basis) for RB (Rayleigh–Bénard). Comput Method Appl Mech Eng 261–262:132–141
5. Patera AT, Rozza G (2006) Reduced basis approximation and a posteriori error estimation for parametrized partial differential equations, Version 1.0, Copyright MIT 2006, (tentative rubric) MIT Pappalardo Graduate Monographs in Mechanical Engineering. Available from: http://augustine.mit.edu/methodology/methodology_bookPartI.htm
6. Chinesta F, Keunings R, Leygue A (2014) The proper generalized decomposition for advanced numerical simulations, springer Briefs in Applied Sciences and Technology. Springer, Berlin
7. Ladevèze P (1989) The large time increment for the analyse of structures with nonlinear constitutive relation described by internal variables. Compt Rend de l'Académie des Sci 309:1095–1099
8. Chinesta F, Leygue A, Beringhier M, Tuan Nguyen L, Grandidier JC, Schrefler B, Pesavento F (2013) Towards a framework for nonlinear thermal models in shell domains. Int J Numer Method Heat Fluid Flow 23(1):55–73
9. Bilasse M, Azrar L, Daya EM (2011) Complex modes based numerical analysis of viscoelastic sandwich plates vibrations. Comput Struct 89:539–555
10. de Lima AMG, da Silva AR, Rade DA, Bouhaddi N (2010) Component mode synthesis combining robust enriched Ritz approach for viscoelastically damped structures. Eng Struct 32:1479–1488
11. Zghal S, Bouazizi ML, Bouhaddi N, Nasri R (2015) Model reduction methods for viscoelastic sandwich structures in frequency and time domains. Finite Elem Anal Design 93:12–29
12. Bilasse M, Oguamanam DCD (2013) Forced harmonic response of sandwich plates with viscoelastic core using reduced-order model. Compos Struct 105:311–318
13. Heyman J, Girault G, Guevel Y, Allery C, Hamdouni A, Cadou JM (2013) Computation of Hopf bifurcations coupling reduced order models and the asymptotic numerical method. Comput Fluids 76:73–85
14. Cadou JM, Potier-Ferry M, Cochelin B (2006) A numerical method for the computation of bifurcation points in fluid mechanics. Eur J Mech B 25:234–254
15. Brezillon A, Girault G, Cadou JM (2010) A numerical algorithm coupling a bifurcating indicator and a direct method for the computation of Hopf bifurcation points in fluid mechanics. Comput Fluids 39:1226–1240
16. Girault G, Guevel Y, Cadou JM (2012) An algorithm for the computation of multiple Hopf bifurcation points based on Padé approximants. Int J Numer Method Fluids 68:1189–1206
17. Cochelin B (1994) A path-following technique via an asymptotic-numerical method. Comput Struct 53(5):1181–1192
18. Cadou JM, Potier-Ferry M (2010) A solver combining reduced basis and convergence acceleration with applications to non-linear elasticity. Int J Numer Method Biomed Eng 26:1604–1617

19. Daya EM, Potier-Ferry M (2002) Finite element for viscoelastically damped sandwich structures. Revue Européenne des Eléments Finis 11:39–56
20. Abdoun F, Azrar L, Daya EM, Potier-Ferry M (2009) Forced harmonic response of viscoelastic structures by an asymptotic numerical method. Comput Struct 87:91–100
21. Duigou L, Daya EM, Potier-Ferry M (2003) Iterative algorithms for non-linear eigenvalue problems. Appl Vib Viscoelastic Shells, Comput Method Appl Mech Eng 192:1323–1335
22. Imazatène A, Cadou JM, Zahrouni H, Potier-Ferry M (2001) A new reduced basis method for non-linear problems. Revue Européenne des Eléments Finis 10(1):55–76
23. Jbilou K, Sadok H (2000) Vector extrapolation methods. Appl Numer Comp J Comput Appl Math 122:149–165
24. Baker GA, Graves-Morris P (1996) Padé approximants, encyclopedia of mathematics and its applications, 2nd edn. Cambridge University Press, Cambridge
25. Damil N, Cadou JM, Potier-Ferry M (2004) Mathematical and numerical connections between polynomial extrapolations and Padé approximants. Commun Numer Method Eng 20(9):699–707
26. Cadou JM, Duigou L, Damil N, Potier-Ferry M (2009) Convergence acceleration of iterative algorithms. Applications to thin shell analysis and Navier-Stokes equations. Comput Mech 43(2):253–264
27. Galliet I, Cochelin B (2004) Une version parallèle des méthodes asymptotiques numériques. Revue Européenne des Eléments Finis 13:177–195
28. Jepson AD (1981) Numerical Hopf bifurcation. Thesis, California Institute of Technology
29. Boumediene F, Duigou L, Boutyour EH, Miloudi A, Cadou JM (2011) Nonlinear forced vibration of damped plates coupling asymptotic numerical method and reduction models. Comput Mech 47(4):359–377
30. Jackson CP (1987) A finite-element study of the onset of vortex shedding in flow past variously shaped body. J Fluid Mech 182:23–45
31. Griewank A, Reddien G (1983) The computation of Hopf points by a direct method. IMA J Numer Anal 3:295–303
32. Bensaadi MEH (1995) Méthode asymptotique-numérique pour le calcul de bifurcations de Hopf et de solutions périodiques. Thesis, Université de Metz
33. Soni ML (1981) Finite element analysis of viscoelastically damped sandwich structures. Shock Vib Bull 55(1):97–109
34. Zienkiewicz OC, Taylor RL (1991) The finite element method, 2, 4th edn. Mcgraw-hill book company, New York
35. Cadou JM, Cochelin B, Damil N, Potier-Ferry M (2001) Asymptotic numerical method for stationary Navier–Stokes equations and with Petrov–Galerkin formulation. Int J Numer Method Eng 50:825–845
36. Wahba EM (2009) Multiplicity of states for two-sided and four-sided lid driven cavity flows. Comput Fluids 38:247–253
37. Cadou JM, Guevel Y, Girault G (2012) Numerical tools for the stability analysis of 2D flows. Appl Two Four-sided Lid-driven Cavity Fluid Dyn Res 44:031403
38. Abouhamza A, Pierre R (2003) A neutral stability curve for incompressible flows in a rectangular driven cavity. Math Comput Model 38:141–157
39. Auteri F, Parolini N, Quartapelle L (2002) Numerical investigation on the stability of singular driven cavity flow. J Comput Phys 183:1–25
40. Boppana VBL, Gajjar JSB (2010) Global flow instability in a lid-driven cavity. Int J Numer Method Fluids 62(8):827–853
41. Fortin A, Jardak M, Gervais JJ, Pierre R (1997) Localization of Hopf bifurcations in fluid flow problems. Int J Numer Method Fluids 24:1185–1210
42. Poliashenko M, Aidun CK (1995) A direct method for computation of simple bifurcations. J Comput Phys 121:246–260
43. Wahba EM (2013) Numerical simulations of flow bifurcations inside a driven cavity. CFD Lett 3(2):100–110
44. Zhuo C, Zhong C, Guo X, Cao J (2013) MRT-LBM simulation of four-lid-driven cavity flow bifurcation. Procedia engineering, 25th international conference on parallel computational fluid dynamics vol 61, pp 100–107
45. Guevel Y, Boutyour H, Cadou JM (2011) Automatic detection and branch switching methods for steady bifurcation in fluid mechanics. J Comput Phys 230(9):3614–3629
46. Büchter N, Ramm E, Roehl D (1994) Three dimensional extension of nonlinear shell formulation based on the enhanced assumed strain concept. Int J Numer Method Eng 37:2551–2568
47. Rao DK (1978) Frequency and loss factor of sandwich beams under various boundary conditions. J Mech Eng Sci 20:271–282
48. Ma BA, He JF (1992) Finite element analysis of viscoelastically damped sandwich plates. J Sound Vib 52:107–123
49. Cadou JM, Damil N, Potier-Ferry M, Braikat B (2004) Projection technique to improve high order iterative correctors. Finite Elem Anal Design 41:285–309
50. Boumediene F, Daya EM, Cadou JM, Duigou L (2015) Forced harmonic response of viscoelastic sandwich beams by a reduction method. Mech Adv Mater Struct. doi:10.1080/15376494.2015.1068408